Chemical Engineering Science 294 (2024) 120082

Contents lists available at ScienceDirect

Chemical Engineering Science

journal homepage: www.elsevier.com/locate/ces

CFD modeling of emulsions inside static mixers

Jody Albertazzi [a], Federico Florit [b], Valentina Busini [a,*], Renato Rota [a]

[a] Politecnico di Milano, Department of Chemistry, Materials and Chemical Engineering "G. Natta", Piazza Leonardo da Vinci 32, 20133, Milano, Italy
[b] Massachusetts Institute of Technology, Department of Chemical Engineering, 77 Massachusetts Ave, Cambridge, MA, 02139, United States of America

ABSTRACT

Emulsification carried out in continuous devices offers a series of advantages over batch emulsion, such as better control of the droplet size distribution, reduced volume equipment, and lower operative costs. This paper investigates through Computational Fluid Dynamics simulations the emulsification process inside Sulzer Static Mixers. An analysis aimed to identify the most appropriate turbulence model, from a practical point of view, was performed, finding that the realizable $k-\epsilon$ model is more suitable than the well-known $k-\omega$ model. Moreover, an operative correlation linking the Sauter diameter to the main operating parameters, in a wide range of fluid properties and operating conditions, was developed.

1. Introduction

Emulsification processes allow the dispersing of one fluid into another almost immiscible fluid in the form of fine droplets (Wang et al., 2023): they are widely used in different industrial fields such as chemical, paint, pharma, food, and contaminant removal (Lei et al., 2022; Naeeni and Pakzad, 2019; Ouda et al., 2020). Emulsions can be produced in batch modes (Al Taweel et al., 2013; Lebaz et al., 2022): however, there is a growing interest in the batch-to-continuous transformation of processes that are normally led discontinuously (Albertazzi et al., 2022; Kimura et al., 2016; Maestri et al., 2020; Puglisi et al., 2015), since a continuous process can offer several advantages with respect to a batch one, such as reduced volumes, increased productivity, and constant quality of the final product (Asua, 2015; Florit et al., 2018, 2019). When it comes to the emulsification process, a continuous operation mode can be adopted when large scales of production are needed (Madhavan et al., 2021).

When using a continuous process, devices such as stirred tanks, rotor-stators, and high-pressure homogenizers can be used (Lebaz et al., 2022; Madhavan et al., 2021). These devices are efficient but a spatially heterogeneous field of breakage may be obtained even with a high power consumption (Klutz et al., 2015; Lebaz et al., 2022). An alternative is represented by static mixers: these are simple mixing elements that can induce turbulence reducing axial dispersion (Aprile et al., 2023; Das et al., 2005), at the cost of higher pressure drops inside the pipe. On the other hand, having no moving parts, they are less susceptible to failures and require lower maintenance, as well as lower operative costs (Klutz et al., 2015; Ouda et al., 2020; Soman and Madhuranthakam, 2017). It was reported in previous works (Albertazzi et al., 2021a,b) that the Sulzer Static Mixers (SMXs) are capable of reaching a very high mixing degree in the radial direction, while at the same time ensuring a negligible value of axial dispersion and dead volumes. Moreover, static mixers are deemed to be effective in water treatment applications (Fleite et al., 2020; Nikooei et al., 2023; Sreedhar et al., 2018), in the recovery of heavy metals from aqueous solutions (Das et al., 2015), as turbulence promoters in ultrafiltration applications (Krstić et al., 2007; Sreedhar et al., 2018; Zhen et al., 2006) and as tools to avoid membrane fouling in dynamic membrane bioreactors (Sabaghian et al., 2018). Static mixers allow the two phases to be mixed through the induced turbulence; this process increases the volumetric mass transfer coefficient $K_L a$, where K_L is the mass transfer coefficient and a is the interfacial area (Das et al., 2015), which in turn depends on the droplet diameters. The breakage process in turbulent flows caused by turbulent fluctuations or by particle-eddy collisions (Liao and Lucas, 2009) is driven by energy dissipation: when the disruptive forces overcome the cohesive forces, the dispersed fluid is broken into droplets therefore creating an emulsion of a fluid into another fluid. These forces are summarized by the Weber number (Eq (1)), which is the ratio between inertial forces and cohesive forces, and the Reynolds number (Eq (2)), which is the ratio between inertial forces and viscous forces (Theron et al., 2010):

$$We_c = \frac{\rho_c \cdot u^2 \cdot D}{\sigma} \tag{1}$$

$$Re_c = \frac{\rho_c \cdot u \cdot D}{\mu_c} \tag{2}$$

* Corresponding author.
E-mail address: valentina.busini@polimi.it (V. Busini).

https://doi.org/10.1016/j.ces.2024.120082
Received 16 January 2024; Received in revised form 28 March 2024; Accepted 1 April 2024
Available online 5 April 2024

Where ρ_c is the continuous phase density, u is the spatial velocity inside the pipe, D is the diameter of the device, σ is the interfacial tension between the fluids and μ_c is the continuous phase viscosity.

In recent years, Computational Fluid Dynamics (CFD) simulations established as powerful tools to study the hydrodynamics inside static mixers, through the modeling of transport phenomena and local fluid dynamics (Albertazzi et al., 2021a,b, 2022; Coroneo et al., 2012; Montante et al., 2016). The properties of an emulsion in CFD simulations can be represented by the Population Balance Model (PBM) (Wang et al., 2005), which is extensively used in the literature to predict Droplet Size Distributions (DSD) during continuous emulsification under different conditions. For example, Lebaz et al. (2022) investigated the continuous emulsification process of silicone oil dispersion into ultrapure water in the SMX focusing on the advantages and limitations of modeling approaches between population balance equation (PBE) versus mean-size correlations. Haddadi et al. (2020) used the PBM to simulate the turbulent dispersion inside Kenics Static Mixers (KSM). Meng et al. (2021) performed numerical simulations of silicone oil-water two-phase turbulent dispersion mixing in Q-type static mixers (QSM) coupling CFD with PBM.

Despite several papers previously presented in literature used CFD to investigate emulsions in static mixers, the influence of different turbulence models on the modeling of emulsification processes inside SMX, has not been studied yet. Therefore, the main aim of this work is to determine which turbulence model is more effective (from a practical point of view) to predict the properties of emulsions inside SMX. Moreover, a general operative correlation able to foresee the SMX performances in a wide range of fluid properties and operating conditions, was developed.

2. Methods

Since thorough mixing of the chemical species is desired, the Eulerian approach was used (Haddadi et al., 2020; Lebaz and Sheibat-Othman, 2019; Meng et al., 2021). The multiphase flows are described as interpenetrating continua, through the concept of volume fraction of the i-th phase (α_i), which is defined as the space percentage occupied by the i-th phase (ANSYS Inc., 2018) and is expressed by (3):

$$V_i = \int_V \alpha_i dV \tag{3}$$

where V_i is the space occupied by phase i. Continuity and momentum conservation equations are:

$$\frac{\partial}{\partial t}(\alpha_i \rho_i) + \nabla \cdot (\alpha_i \rho_i u_i) = 0 \tag{4}$$

$$\frac{\partial}{\partial t}(\alpha_i \rho_i u_i) + \nabla \cdot (\alpha_i \rho_i (u_i u_i)) = -\alpha_i \nabla p + \alpha_i \rho_i g + \nabla \cdot \tau_i + F \tag{5}$$

where ρ_i and u_i are the density and the velocity for the i-th phase, respectively; p is the pressure, τ_i is the i^{th} phase stress-strain tensor and F is the interfacial force term. F is given by the sum of three phase-weighted contributions, which are the drag force (F_d), the lift force (F_l), and the virtual mass force (F_v), respectively. The lift term plays a minor role compared to the drag force and can be neglected (ANSYS Inc., 2018), while the virtual mass effect becomes significant only when the secondary phase density is much smaller than the continuous phase density (ANSYS Inc., 2018); therefore, in this work, only the drag force was considered.

The drag force was modeled using the Schiller and Neumann method, which is acceptable for all fluid-fluid pairs of phases (ANSYS Inc., 2018):

$$F_d = \alpha_c \alpha_d \cdot \left(\frac{3}{4} C_D \cdot \frac{\rho_d}{d} |u_d - u_c| \right) \cdot (u_d - u_c) \tag{6}$$

$$C_D = \begin{cases} \frac{24}{Re_r} \cdot (1 + 0.15 \cdot Re_r^{0.687}) & Re_r \leq 1000 \\ 0.44 & Re_r > 1000 \end{cases} \tag{7}$$

$$Re_r = \frac{\rho_c d \cdot |u_d - u_c|}{\mu_c} \tag{8}$$

where d is the droplet diameter, C_D is the drag coefficient, Re_r is the relative Reynolds number, and the subscripts c and d refer to the continuous and dispersed phases, respectively.

2.0.1. Turbulence model

Static mixers are capable of inducing high local turbulence levels even for low values of Re (Albertazzi et al., 2021a,b). Therefore, modeling the near-wall area is of great importance and impacts the reliability of the numerical solution, since walls significantly influence the turbulence production in bounded flows (ANSYS Inc., 2018). Two modeling approaches are commonly used; in the first approach the viscosity-affected inner region is not directly solved, but wall functions are used to link the viscosity-affected region and the fully turbulent region using semi-empirical relations called wall functions. The main disadvantage of the wall functions approach is that the numerical solution tends to become less accurate under grid refinement in the normal direction; in particular, low values of dimensionless distance from the walls can lead to divergence of the numerical method as a consequence of extremely large values of shear stress and heat transfer (ANSYS Inc., 2018). The dimensionless distance can be defined as $y^* \equiv \frac{\rho C_\mu^{1/4} k_P^{1/2} y_P}{\mu}$ where C_μ is a model constant equal to 0.09, k_P is the turbulence kinetic energy at the wall-adjacent cell centroid, y_P is the distance from the centroid of the wall-adjacent cell to the wall and ρ and μ are the density and the dynamic viscosity of the fluid or as $y^+ = \frac{\rho \sqrt{\tau_w/\rho} y}{\mu}$, where τ is the shear stress in an arbitrary layer of fluid (ANSYS Inc., 2018). However, the scalable wall functions approach allows to obtain consistent results also for refined grids through the introduction of a limiter, such that $\tilde{y}^* = MAX(y^*, y^*_{limit})$ where $y^*_{limit} \approx 11.225$ (ANSYS Inc., 2018). The second approach solves the near-wall region without using wall functions; this allows to obtain results independent of the grid refinement close to the wall, which is the approach behind the $k-\omega$ family of turbulence models. However, this approach requires high grid resolution of the boundary layer.

2.0.2. Population balance model

In this work, the Population Balance Model was solved through the discrete method. This method is based on representing the continuous particle size distribution in terms of a set of discrete size classes and allows to easily obtain the Droplet Size Distribution (DSD) with ease and with good robustness (Meng et al., 2021). The droplets are categorized according to their volume ratio. Assuming the droplets as spherical, the volume ratio of each class is $V_i/V_{i+1} = 2^k$. The higher k, the wider the range of diameters for a given number of bin sizes. In this work, k was kept equal to 1 to have a more precise distribution of the bin sizes. The transport equation for the number density function is given by Hagesaether et al. (2002a); Naeeni and Pakzad (2019):

$$\frac{\partial}{\partial t}[n(V,t)] + \nabla \cdot [u \times n(V,t)] = S(V,t) \tag{9}$$

where V is the droplet volume, t is the time, $n(V,t)$ is the number density function, u is the velocity vector of the droplet, and $S(V,t)$ is the term accounting for the droplet breakage and coalescence defined as:

$$S_i = (B_C - D_C + B_B - D_B)_i \tag{10}$$

$(B_C)_i$ represents the birth rate of droplets by coalescence, $(D_C)_i$ the death rate of droplets by coalescence, $(B_B)_i$ the birth rate of droplets by breakage and $(D_B)_i$ the death rate of droplets by breakage. Assuming no breakup of the smallest droplet size ($i = 1$) and no coalescence in the largest class ($i = N$) the terms for birth and death of droplets for breakage are defined as Hagesaether et al. (2002a):

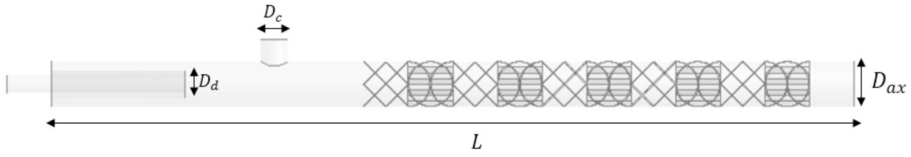

Fig. 1. Side view of the pipe.

$$B_B(i) = \sum_{k=i+1,i\neq N}^{N} \Omega_B(V_k, V_i) + \sum_{k=i,i\neq N}^{i} x_{i+1,k}\Omega_B(V_{i+1}, V_k) + \sum_{k=i,i\neq 1}^{i-1} (1 - x_{i,k})\Omega_B(V_i, V_k), i = 1, ..., N \quad (11)$$

$$D_B(i) = \sum_{k=1}^{i-1} \Omega_B(V_i, V_k), i = 2, ..., N \quad (12)$$

where the term $\Omega_B(V_i, V_k)$ is the breakage rate of a particle of volume V_i into a particle of volume V_k. To predict the breakage (or kernel) rate, different models are available in the literature (Ghadiri and Zhang, 2002; Luo and Svendsen, 1996; Nambiar et al., 1992). In this work, the Luo and Lehr model (ANSYS Inc., 2009) was used for both the breakage frequency and the PDF of breaking particles. The breakage rate is defined as:

$$\Omega_B(V_i, V_k) = K \int_{\xi_{min}}^{1} \frac{(1+\xi)^2}{\xi^n} exp(-b\xi^m) d\xi \quad (13)$$

where ξ is the dimensionless eddy size, K, n, b, and m are model parameters: $K = 0.9238\epsilon^{1/3}d^{-2/3}\alpha$, ϵ is the turbulent dissipation rate energy, α is dispersed phase volume fraction, $m = -11/3$, $b = \frac{-12c_f\sigma}{\beta\rho_c\epsilon^{2/3}d^{5/3}}$, $\beta = 2$, $c_f = f_{BV}^{2/3} + (1 - f_{BV})^{2/3} - 1$, where σ and f_{BV} are the interfacial tension and the breakage volume fraction (that is, the proportion of droplets that have ruptured), respectively (ANSYS Inc., 2009).

The droplet birth and death rate due to coalescence are defined as Hagesaether et al. (2002b):

$$B_C(i) = \sum_{j=i,i\neq N}^{i-1} x_{i,j}\Omega_C(V_i, V_j) + \sum_{j=i}^{i-1} (1 - x_{i-1,j})\Omega_C(V_{i-1}, V_j), i = 2, ..., N \quad (14)$$

$$D_C(i) = \sum_{j=1}^{N-1} \Omega_C(V_i, V_j) + \Omega_C(V_i, V_i), i = 1, ..., N-1 \quad (15)$$

The aggregation kernel is represented by the product of two different terms: the frequency of collisions between particles of volume V_i and volume V_j, and the efficiency of aggregation (that is, the probability of particles of volume V_i coalescing with particles with volume V_j). To model the aggregation kernel, the turbulent model was chosen, since it can simulate both the viscous subrange mechanism (applied to all the molecules smaller than the Kolmogorov microscale ν) and the inertial subrange mechanism (applied to all the molecules bigger than ν (ANSYS Inc., 2009)). This model proved to be effective in the modeling of the coalescence of droplets in oil-water mixtures (Luo and Svendsen, 1996) and has been used in similar works involving static mixers in turbulent flows (Meng et al., 2021).

For the viscous subrange, particle collisions are influenced by the local shear within the eddy, and the collision rate is expressed as:

$$\Omega_C(V_i, V_j) = \zeta_T \sqrt{\frac{8\pi}{15}} \dot{\gamma} \frac{(d_i + d_j)^3}{8} \quad (16)$$

where $\dot{\gamma}$ is the shear rate ($\dot{\gamma} = \epsilon^{0.5}/\nu$) and ζ_T is a factor that takes into account the capture efficiency of turbulence collision and is defined through the following:

Table 1
Geometrical properties of reactor [cm].

D_{ax}	L	D_d	D_c
1	17	0.4	0.6

Table 2
Operating conditions and fluid properties used for the mesh independence analysis.

ρ_C $\left[\frac{kg}{m^3}\right]$	ρ_D $\left[\frac{kg}{m^3}\right]$	μ_C [cP]	μ_D [cP]	$\dot{m}_C$ $\left[\frac{kg}{s}\right]$	$\dot{m}_D$ $\left[\frac{kg}{s}\right]$
995	770	0.001	0.0009	0.042	0.0108

$$\zeta_T = 0.732\left(\frac{5}{N_T}\right), N_T \geq 5 \quad (17)$$

In the previous relation, N_T is the ratio between the viscous forces and the Van der Waals forces, defined as $N_T = \frac{6\pi\mu(d_i+d_j)^3\dot{\lambda}}{8H}$, with H and $\dot{\lambda}$ being the Hamaker constant and the deformation rate, respectively. Considering the inertial subrange, the aggregation rate is expressed as:

$$\Omega_C(V_i, V_j) = \zeta_T 2^{3/2}\sqrt{\pi}\frac{(d_i + d_j)^2}{4}\sqrt{(U_i^2 + U_j^2)} \quad (18)$$

where d_i and d_j are the sizes of the particles i and j respectively and U_i is the mean squared velocity for the particle i.

2.1. Mesh

2.1.1. Integration domain

The integration domain consists of a pipe equipped with Sulzer Static Mixers, as shown in Fig. 1. The pipe is packed with 10 static mixers each with a length-to-diameter ratio equal to 1. Each element is composed by eight crossed bars, rotated by 90° one to each other; moreover, to enhance the mixing, each static mixer is rotated by 90° with respect to the previous one. The diameter of the axial tube (D_{ax}) is equal to 1 cm. The continuous phase (c) is fed into the pipe through a lateral tube, with a diameter $D_c = 0.6$ cm, while the dispersed phase (d) enters through an axial tube, with a diameter $D_d = 0.4$ cm. The modeled geometry is summarized in Table 1.

2.1.2. Grid independence

The continuity, momentum, volume fraction and population balance equations (PBE) were solved through Ansys Fluent 19.1, using a RANS approach (ANSYS Inc., 2018) with a second-order upwind and a QUICK scheme. The three-dimensional geometry shown in Fig. 1 was discretized into a series of polyhedral cells; this type of cell has been proven to be effective in improving the computational efficiency (Achermann et al., 2022; Meng et al., 2021). The orthogonal quality was kept higher than 0.1 for all the cells, to ensure high quality in the resulting mesh. A mesh independence analysis was performed, through a series of simulations with increasing number of computational cells; the operating conditions for this set of simulations are summarized in Table 2.

The Sauter diameter at the exit of the last static mixer, defined as $d_{32} = \frac{\sum N_i d_i^3}{\sum N_i d_i^2}$ was chosen as the characteristic drop size and was used to

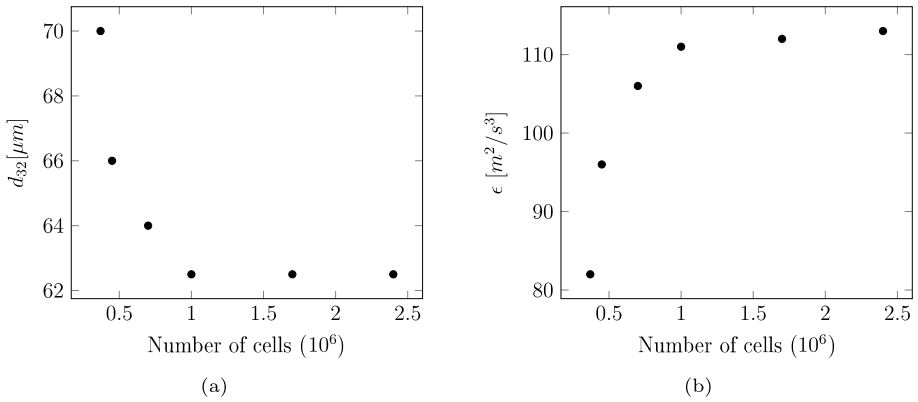

Fig. 2. Mesh independence analysis. Sauter diameter (d_{32}) as a function of the number of cells (a); turbulent dissipation rate (ϵ) as a function of the number of cells (b).

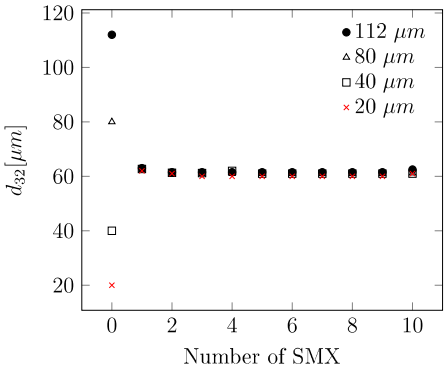

Fig. 3. Sauter diameter as a function of the number of static mixers for different inlet bin diameters.

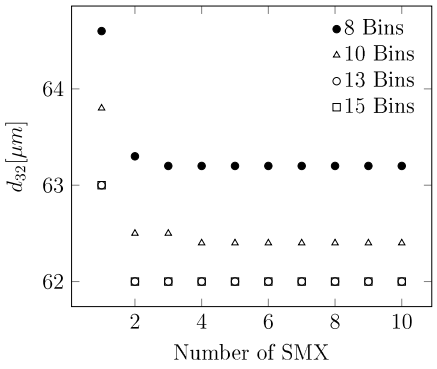

Fig. 4. Sauter diameter as a function of the number of static mixers for different inlet bin numbers.

compare the results obtained with the different meshes. It is possible to see from the results, shown in Fig. 2a that the predicted d_{32} values decrease when the number of cells increases from up to about 10^6 cells; above this value, there is no significant change in the d_{32} values. This trend is also confirmed by the values of volume averaged turbulent dissipation rate (ϵ) shown in Fig. 2b. In this work, a mesh composed of 1.7 Million cells was used.

2.1.3. Inlet droplet diameter and droplet class size

The population balance model needs the particle diameters at the inlet of the dispersed phase to be discretized in a series of bins. To assess the influence of the inlet size distribution on the Sauter diameter at the exit of SMX, several simulations were carried out with different average inlet diameters. The volume fraction, defined as $\alpha = Q_d/(Q_c + Q_d)$, where Q_c and Q_d are the continuous phase volumetric flow rate and the dispersed phase volumetric flow rate, was kept constant and equal to $\alpha = 0.25$. The droplet diameters ranged between 20×10^{-6} m and 1.12×10^{-4} m, whereas the number of bins was kept equal to 13. Results are reported in Fig. 3, where the Sauter diameter computed at the exit of different numbers of SMX is summarized. It can be seen that after the first mixing element, $d_{32} \approx 60\ \mu m$ regardless of the inlet Sauter diameter. This means that the breakage and the coalescence of the dispersed phase droplet inside the SMX is not influenced significantly by the inlet size distribution, as already reported in the literature (Meng et al., 2021).

To investigate the influence of the number of bin classes a few simulations were carried out with an inlet d_{32} equal to 20 μm. The main results are shown in Fig. 4: we can see that the results obtained using 13 and 15 bins overlap. Therefore, in all the simulations the inlet particle diameters were discretized in 13 bins.

3. Results and discussion

3.1. Influence of the turbulence model choice

Turbulence modeling is of paramount importance when dealing with emulsions, since the dissipated turbulent energy ϵ is the main force driving the breakage of the dispersed phase droplets. A set of simulations were performed using both the SST $k-\omega$ and the realizable $k-\epsilon$ models and the predicted Sauter diameters were compared to the experimental results obtained by Theron et al. (2010) using a 1 cm pipe diameter equipped with 10 SMX as reported in Fig. 1. The realizable $k-\epsilon$ model was chosen since it can accurately model strongly swirling flows, typical of static mixers (Lebaz et al., 2022). The continuous phase (c) was water-Tween 80 (1.5% weight) and the dispersed phase (d) was cyclohexane. The densities of the two phases are equal to $\rho_c = 995\,\mathrm{kg/m^3}$ and $\rho_d = 770\,\mathrm{kg/m^3}$, while their viscosities $\mu_c = 1 \cdot 10^{-3}$ Pa · s and $\mu_d = 9 \cdot 10^{-4}$ Pa · s. In all the simulations the volume fraction was considered equal to $\alpha = 0.25$ and the interfacial tension was kept equal to $\sigma = 0.003$ N/m. The other operating conditions are summarized in Table 3.

Fig. 5a compares the Sauter diameters measured after 10 static mixers (Theron et al., 2010) with the simulations performed using the realizable $k-\epsilon$ model and the SST $k-\omega$ model as a function of the Re number. We can see that when using the same number of cells, the realizable $k-\epsilon$ model can effectively foresee the emulsification processes inside static mixers with a higher accuracy with respect to the SST $k-\omega$ model. The reason is that the realizable $k-\epsilon$ model is specifically designed to reproduce complex flows with strong streamline curvatures (Lebaz et al., 2022), as usually found in static mixers.

It should be stressed that this does not mean that the SST $k-\omega$ model cannot reproduce emulsification processes, but that it would re-

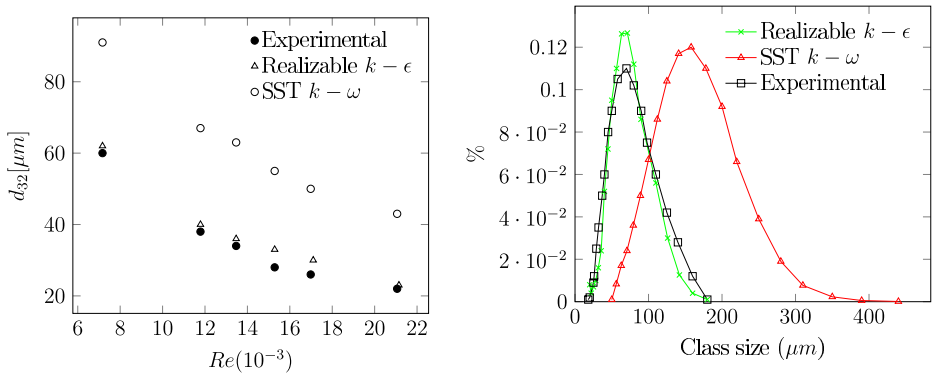

Fig. 5. Sauter diameters as a function of Re number (a); DSD comparison (Q = 204 L/h) (b).

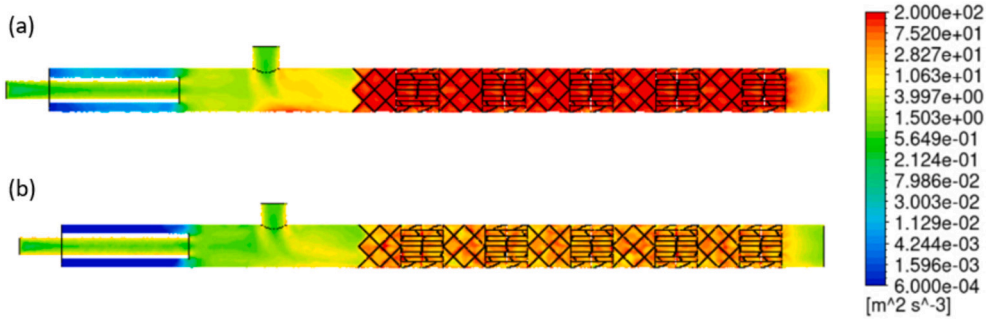

Fig. 6. Contours of turbulence dissipation rate energy measured on the xy plane for the realizable $k-\epsilon$ model (a) and the SST $k-\omega$ model (b).

Table 3
Operating conditions for turbulence model analysis.

$\dot{m}_C\left[\frac{kg}{s}\right]$	$\dot{m}_D\left[\frac{kg}{s}\right]$	Re
0.0422	0.0109	7167
0.0694	0.0180	11787
0.793	0.0206	13469
0.090	0.0234	15286
0.100	0.0260	16985
0.124	0.0320	21061

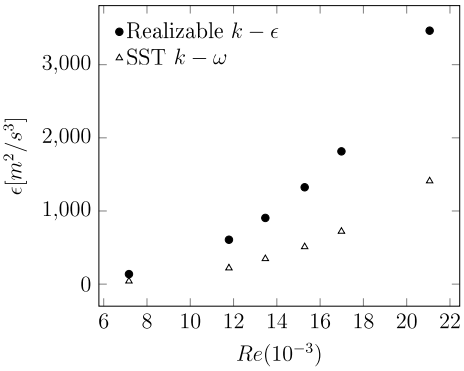

Fig. 7. Values of volume averaged turbulence dissipation rate ϵ obtained with realizable $k-\epsilon$ model and SST $k-\omega$ model for different Re values.

quire a much larger number of cells, as discussed in the following. Moreover, the droplet size distribution obtained at Q = 204 L/h with the realizable k-ϵ model was measured and compared with the one obtained with the SST k-ω model and with the experimental data. It is possible to see in Fig. 5b that, while the realizable k-ϵ model approaches reasonably well the experimental data, there is a huge difference when the SST k-ω model is considered, confirming the results previously shown.

The contours of the volume-averaged turbulence dissipation rate were computed by the two turbulence methods as shown in Fig. 6 for a typical run. We can see that the turbulence dissipation rate energy computed by the realizable $k-\epsilon$ is higher than that computed through the SST $k-\omega$.

These visual results are confirmed by Fig. 7 which shows the turbulence dissipation rate for various simulations carried out with both the realizable $k-\epsilon$ and SST $k-\omega$ model.

The reason for such a difference can be understood by looking at the y^+ values predicted by the SST $k-\omega$ on the static mixers walls, as shown in Fig. 8; close to the mixing elements wall the y^+ value is higher than 5, therefore leading to numerical errors in the modeling of the turbulent rate close to the static mixers walls, which strongly affect the droplet size diameters. This problem could be solved by using a mesh with a higher number of cells close to the walls (ANSYS Inc., 2018) but at the cost of a much higher computational time. To validate this claim, simulations at $Re = 21146$ were repeated with the SST k-ω model with 7,9 and 12 million cells. The results summarized in Table 4 show that it is possible to obtain results closer to the experimental data. However, the residual values obtained with the SST $k-\omega$ model were higher than $1 \cdot 10^{-2}$, suggesting that a much thicker mesh should be used to obtain reliable results, and the computational time was roughly 5 times higher, therefore candidating the realizable $k-\epsilon$ model as the preferred tool from a practical point of view.

3.2. Correlation

As a practical engineering tool for predicting the d_{32} value induced by SMX, a general correlation based on literature experimental data (Kiss et al., 2011; Rao et al., 2007; Theron et al., 2010) as well as on several CFD simulations carried out in this work was developed. The Sauter droplet diameters depend on the physical properties of the fluids and the geometrical properties of the static mixers. Among the others, the following properties are expected to play a relevant role in defining the d_{32} value (Kiss et al., 2011):

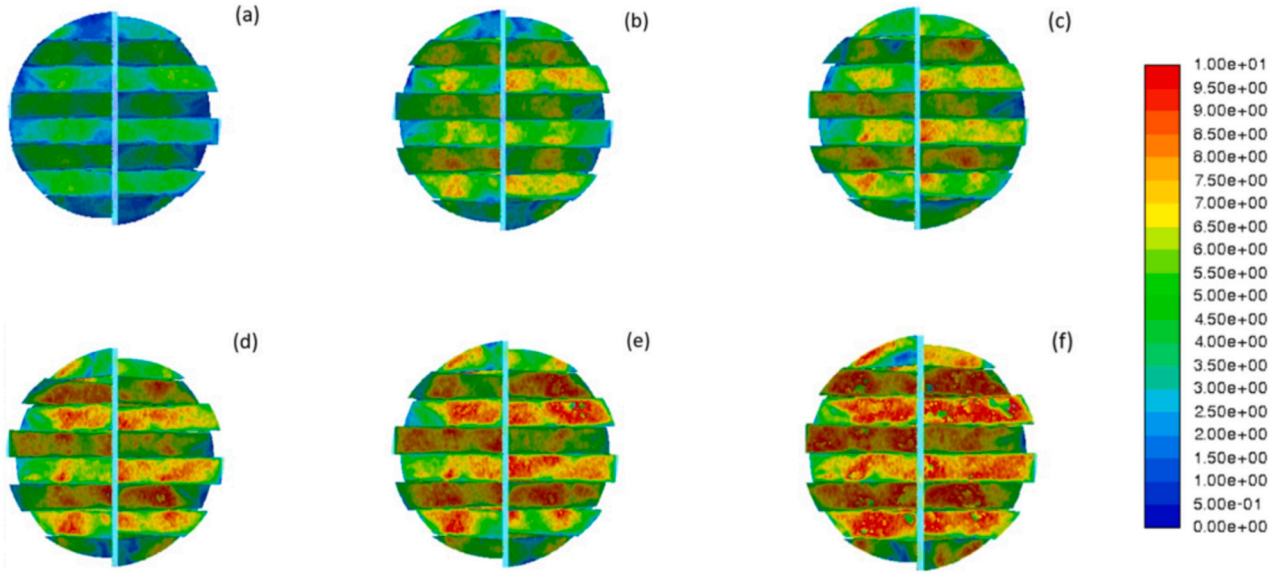

Fig. 8. Contour of wall Y^+ obtained with the SST $k-\omega$ model for: (a) $Re = 7167$; (b) $Re = 11787$; (c) $Re = 13469$; (d) $Re = 15286$; (e) $Re = 16985$; (f) $Re = 21061$.

Table 4
Sauter diameters and percentage error obtained with realizable $k-\epsilon$ and SST $k-\omega$ models for different meshes.

//	d_{32} [μm]	η [%]
Experimental	21	0
$k-\epsilon, 1.7Mln$	23	9.5
$k-\omega, 1.7Mln$	43	104
$k-\omega, 7Mln$	36	71
$k-\omega, 9Mln$	33	60
$k-\omega, 12Mln$	30	42

Table 5
Operating ranges of the data summarized in Fig. 9.

$\frac{\mu_d}{(\rho_d D\sigma)^{0.5}}$	$\frac{u}{\mu_d\sigma}$	$\frac{\rho_c}{\rho_d}$	$\frac{\mu_c}{\mu_d}$	α	N_{SMX}
0.0059 – 1.26	0.21 – 7.41	1.00 – 1.37	0.018 – 1.11	0.01 – 0.25	6 – 10

$$d_{32} = f(u, D, L, \mu_c, \mu_d, \rho_c, \rho_d, \alpha, \sigma) \tag{19}$$

where u is the superficial velocity, computed considering the total flow rate entering the pipe, D the pipe diameter, L the pipe length, μ_c the continuous phase viscosity, μ_d the dispersed phase viscosity, ρ_c the continuous phase density, ρ_d the dispersed phase density, α the volume fraction of the dispersed phase and σ the interfacial tension. Combining these parameters, we can obtain seven dimensionless groups, following a procedure similar to the one discussed in the work by Kiss et al. (2011): two Ohnesorge numbers ($\frac{\mu_d}{(\rho_d d_{32}\sigma)^{0.5}}$ and $\frac{\mu_d}{(\rho_d D\sigma)^{0.5}}$), the Capillary number, $\frac{u}{\mu_d\sigma}$, the number of mixing elements (N_{SMX}), the viscosity ratio (μ_c/μ_d), the density ratio (ρ_c/ρ_d) and the volume fraction (α). A simple polynomial correlation was used, whose constant and exponents were determined by multiple regression fitting with the operating window summarized in Table 5.:

$$\frac{\mu_d}{(\rho_d d_{32}\sigma)^{0.5}} = 2.205 \cdot \left(\frac{\mu_d}{(\rho_d D\sigma)^{0.5}}\right)^{0.72} \cdot \left(\frac{u}{\mu_d\sigma}\right)^{0.24} \cdot \left(\frac{\rho_c}{\rho_d}\right)^{-1.4} \cdot \left(\frac{\mu_c}{\mu_d}\right)^{0.12} \cdot \alpha^{-0.22} \cdot N_{SMX}^{0.4} \tag{20}$$

The exponents obtained for the dimensionless groups $\frac{\mu_d}{(\rho_d D\sigma)^{0.5}}$, $\frac{u}{\mu_d\sigma}$ and $\frac{\mu_c}{\mu_d}$ are similar to the ones already obtained by Kiss et al. (2011).

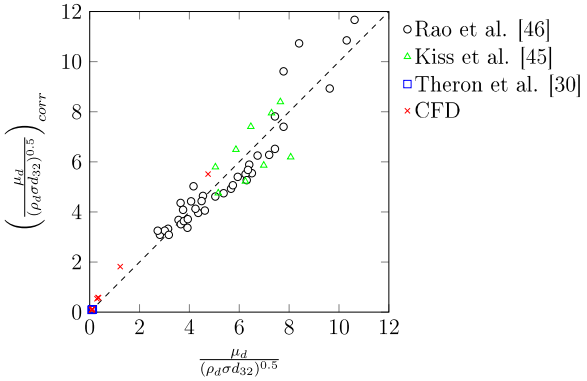

Fig. 9. Dimensionless Sauter diameter values computed through eq (19) vs literature (Kiss et al., 2011; Rao et al., 2007; Theron et al., 2010) and CFD simulations results.

However, the proposed correlation expands the range of operating conditions and considers also the influence of N_{SMX} and $\frac{\rho_c}{\rho_d}$.

Fig. 9 shows in a parity plot the performances of the proposed correlation when compared with the dimensionless Sauter diameter both from literature (Kiss et al., 2011; Rao et al., 2007; Theron et al., 2010) and this work. The values predicted by the correlation (eq (19)) have a coefficient of determination $R^2 = 0.93$. From this figure we can see that the proposed correlation can reasonably predict the experimental/CFD results in the investigated operating window.

4. Conclusions

In this work, the CFD modeling of emulsions inside SMX was discussed. It was found that: the values of d_{32} predicted using the $k-\omega$ SST are highly susceptible to the values of y^+ in the near-wall region, therefore requiring a huge number of cells to predict the Sauter diameters leaving the mixing elements. On the other hand, the realizable $k-\epsilon$ model can predict the emulsification process inside the SMX static mixers with a much lower number of cells. From CFD simulations, carried out together with several experimental results previously reported in the literature, a practical correlation valid for a wide range of operating conditions was developed to predict the SMX performance in terms of d_{32} value. This work focused on the modeling of emulsions inside static mixers without considering mass transfer between the phases, which

can affect the droplet size distribution (Lan et al., 2016; Wang et al., 2020). Therefore, the developed correlation can be used as a preliminary tool to assess the effectiveness of SMX in mixing multiphase flows.

CRediT authorship contribution statement

Jody Albertazzi: Writing – original draft, Software, Methodology, Investigation, Conceptualization. **Federico Florit:** Conceptualization, Methodology. **Valentina Busini:** Conceptualization, Data curation, Methodology, Supervision, Writing – review & editing. **Renato Rota:** Conceptualization, Formal analysis, Methodology, Supervision, Writing – review & editing.

Declaration of competing interest

The authors declare that they have no known competing financial interests or personal relationships that could have appeared to influence the work reported in this paper.

Data availability

Data will be made available on request.

References

Achermann, R., Adams, R., Prasser, H.-M., Mazzotti, M., 2022. Characterization of a small-scale crystallizer using cfd simulations and x-ray ct measurements. Chem. Eng. Sci. 256, 117697.

Al Taweel, A., Azizi, F., Sirijeerachai, G., 2013. Static mixers: effective means for intensifying mass transfer limited reactions. Chem. Eng. Process.: Process Intensif. 72, 51–62.

Albertazzi, J., Florit, F., Busini, V., Rota, R., 2021a. Mixing efficiency and residence time distributions of a side-injection tubular reactor equipped with static mixers. Ind. Eng. Chem. Res. 60, 10595–10602.

Albertazzi, J., Florit, F., Busini, V., Rota, R., 2021b. Influence of buoyancy effects on the mixing process and rtd in a side-injection reactor equipped with static mixers. Ind. Eng. Chem. Res. 60, 16490–16497.

Albertazzi, J., Florit, F., Busini, V., Rota, R., 2022. A novel static mixer for photochemical reactions. Chem. Eng. Process.: Process Intensif. 182, 109201.

ANSYS Inc., 2009. ANSYS FLUENT 12.0 Population Balance Manual.

ANSYS Inc., 2018. ANSYS Fluent Theory Guide - release 19.1.

Aprile, G., Pandit, A.V., Albertazzi, J., Eren, A., Capellades, G., Thorat, A.A., Gamekkanda, J.C., Vetter, T., Skovby, T., Sin, G., Wu, H., Dam-Johansen, K., Myerson, A.S., 2023. Loop-configuration for plug flow crystallization process development. Cryst. Growth Des. 23 (11), 8052–8064.

Asua, J.M., 2015. Challenges and opportunities in continuous production of emulsion polymers: a review. Macromol. React. Eng. 10, 311–323.

Coroneo, M., Montante, G., Paglianti, A., 2012. Computational fluid dynamics modeling of corrugated static mixers for turbulent applications. Ind. Eng. Chem. Res. 51 (49), 15986–15996.

Das, D., Juvekar, V., Ramprasad, K., Bhattacharya, R., 2015. Comparison of solvent extraction and lem extraction in static mixer for recovery of mo(vi) from dilute aqueous solution. Chem. Eng. Process.: Process Intensif. 95, 372–382.

Das, P.K., Legrand, J., Morançais, P., Carnelle, G., 2005. Drop breakage model in static mixers at low and intermediate Reynolds number. Chem. Eng. Sci. 60 (1), 231–238.

Fleite, S.N., García, A.R., De los Santos, C.N., de Iorio, A.F., Cassanello, M., 2020. Static mixer continuous chemical coagulation–flocculation for cattle feedlot wastewater treatment. Desalination and Water Treatment 189, 98–107.

Florit, F., Busini, V., Storti, G., Rota, R., 2018. From semi-batch to continuous tubular reactors: a kinetics-free approach. Chem. Eng. J. 354, 1007–1017.

Florit, F., Busini, V., Storti, G., Rota, R., 2019. Kinetics-free transformation from non-isothermal discontinuous to continuous tubular reactors. Chem. Eng. J. 373, 792–802.

Ghadiri, M., Zhang, Z., 2002. Impact attrition of particulate solids. Part 1: a theoretical model of chipping. Chem. Eng. Sci. 57 (17), 3659–3669.

Haddadi, M., Hosseini, S., Rashtchian, D., Ahmadi, G., 2020. Cfd modeling of immiscible liquids turbulent dispersion in kenics static mixers: focusing on droplet behavior. Chin. J. Chem. Eng. 28 (2), 348–361.

Hagesaether, L., Jakobsen, H.A., Svendsen, H.F., 2002a. A model for turbulent binary breakup of dispersed fluid particles. Chem. Eng. Sci. 57 (16), 3251–3267.

Hagesaether, L., Jakobsen, H.A., Svendsen, H.F., 2002b. Modeling of the dispersed-phase size distribution in bubble columns. Ind. Eng. Chem. Res. 41 (10), 2560–2570.

Kimura, H., Tomatsu, K., Saiki, H., Arimitsu, K., Ono, M., Kawashima, H., Iwata, R., Nakanishi, I., Ozeki, E., Kuge, Y., Saji, H., 2016. Continuous-flow synthesis of n-succinimidyl 4-[18f] fluorobenzoate using a single microfluidic chip. PLoS ONE 11, e0159303.

Kiss, N., Brenn, G., Pucher, H., Wieser, J., Scheler, S., Jennewein, H., Suzzi, D., Khinast, J., 2011. Formation of o/w emulsions by static mixers for pharmaceutical applications. Chem. Eng. Sci. 66 (21), 5084–5094.

Klutz, S., Kurt, S.K., Lobedann, M., Kockmann, N., 2015. Narrow residence time distribution in tubular reactor concept for Reynolds number range of 10–100. Chem. Eng. Res. Des. 95, 22–33.

Krstić, D.M., Höflinger, W., Koris, A.K., Vatai, G.N., 2007. Energy-saving potential of cross-flow ultrafiltration with inserted static mixer: application to an oil-in-water emulsion. Sep. Purif. Technol. 57 (1), 134–139.

Lan, W., Wang, C., Guo, X., Li, S., Luo, G., 2016. Study on the transient interfacial tension in a microfluidic droplet formation coupling interphase mass transfer process. AIChE J. 62 (7), 2542–2549.

Lebaz, N., Sheibat-Othman, N., 2019. A population balance model for the prediction of breakage of emulsion droplets in smx+ static mixers. Chem. Eng. J. 361, 625–634.

Lebaz, N., Azizi, F., Sheibat-Othman, N., 2022. Modeling droplet breakage in continuous emulsification using static mixers in the framework of the entire spectrum of turbulent energy. Ind. Eng. Chem. Res. 61 (1), 541–553.

Lei, H., Guan, X., Yan, H., 2022. A novel design of in-line static mixer for permanganate/bisulfite process: numerical simulations and pilot-scale testing. Water Environ. Res. 94, e10725.

Liao, Y., Lucas, D., 2009. A literature review of theoretical models for drop and bubble breakup in turbulent dispersions. Chem. Eng. Sci. 64 (15), 3389–3406.

Luo, H., Svendsen, H.F., 1996. Theoretical model for drop and bubble breakup in turbulent dispersions. AIChE J. 42, 1225–1233.

Madhavan, N., Yalla, E., Pushpavanam, S., Renganathan, T., Mukherjee, M., Basavaraj, M.G., 2021. Semi-batch and continuous production of pickering emulsion via direct contact steam condensation. Soft Matter, 9636.

Maestri, F., Copelli, S., Barozzi, M., Rota, R., 2020. Kinetic-free discontinuous to continuous transformation of fine chemical reactions: a general experimental procedure. Chem. Eng. J. 395, 125061.

Meng, H., Wang, J., Yu, Y., Wang, Z., Wu, J., 2021. Cfd–pbm numerical study on liquid–liquid dispersion in the q-type static mixer. Ind. Eng. Chem. Res. 60 (49), 18121–18135.

Montante, G., Coroneo, M., Paglianti, A., 2016. Blending of miscible liquids with different densities and viscosities in static mixers. Chem. Eng. Sci. 141, 250–260.

Naeeni, S.K., Pakzad, L., 2019. Droplet size distribution and mixing hydrodynamics in a liquid–liquid stirred tank by cfd modeling. Int. J. Multiph. Flow 120, 103100.

Nambiar, D., Kumar, R., Das, T., Gandhi, K., 1992. A new model for the breakage frequency of drops in turbulent stirred dispersions. Chem. Eng. Sci. 47 (12), 2989–3002.

Nikooei, E., AuYeung, N., Lima, I., Tan, X., Benard, A., Abbasi, B., 2023. Separation of volatile organic contaminants from water using a direct-contact dehumidifier: an experimental study and modeling. J. Water Proc. Eng. 52, 103520.

Ouda, M., Al-Ketan, O., Sreedhar, N., Hasan Ali, M.I., Abu Al-Rub, R.K., Hong, S., Arafat, H.A., 2020. Novel static mixers based on triply periodic minimal surface (tpms) architectures. J. Environ. Chem. Eng. 8 (5), 104289.

Puglisi, A., Benaglia, M., Porta, R., Coccia, F., 2015. Organocatalysis chemistry in flow. Current Organocatalysis 2, 79–101.

Rao, N. Rama, Baird, M., Hrymak, A., Wood, P., 2007. Dispersion of high-viscosity liquid–liquid systems by flow through smx static mixer elements. Chem. Eng. Sci. 62 (23), 6885–6896.

Sabaghian, M., Mehrnia, M.R., Esmaieli, M., Nourmohammadi, D., 2018. Influence of static mixer on the formation and performance of dynamic membrane in a dynamic membrane bioreactor. Sep. Purif. Technol. 206, 324–334.

Soman, S.S., Madhuranthakam, C.M.R., 2017. Effects of internal geometry modifications on the dispersive and distributive mixing in static mixers. Chem. Eng. Process.: Process Intensif. 122, 31–43.

Sreedhar, N., Thomas, N., Al-Ketan, O., Rowshan, R., Hernandez, H., Abu Al-Rub, R.K., Arafat, H.A., 2018. 3d printed feed spacers based on triply periodic minimal surfaces for flux enhancement and biofouling mitigation in ro and uf. Desalination 425, 12–21.

Theron, F., Le Sauze, N., Ricard, A., 2010. Turbulent liquid-liquid dispersion in sulzer smx mixer. Ind. Eng. Chem. Res. 49, 623–632.

Wang, B., Zhou, H., Yu, X., Jing, S., Zheng, Q., Lan, W., Li, S., 2020. Determination of dynamic interfacial tension in a pulsed column under mass transfer condition. AIChE J. 66 (8), e16257.

Wang, L., Marchisio, D., Vigil, R., Fox, R., 2005. Cfd simulation of aggregation and breakage processes in laminar Taylor–Couette flow. J. Colloid Interface Sci. 282 (2), 380–396.

Wang, Y., Ai, C., Wang, H., Chen, C., Tenh, H., Xiao, J., Chen, L., 2023. Emulsion and its application in the foodfield: an update review. eFood 4, e102.

Zhen, X. hua, Yu, S. li, Wang, B. fu, Zheng, H. feng, 2006. Flux enhancement during ultrafiltration of produced water using turbulence promoter. J. Environ. Sci. 18 (6), 1077–1081.